

The Flying Anemometer: Unified Estimation of Wind Velocity from Aerodynamic Power and Wrenches

Teodor Tomić¹, Korbinian Schmid², Philipp Lutz¹, Andrew Mathers³, and Sami Haddadin⁴

Abstract—We consider the problem of estimating the wind velocity perceived by a flying multicopter, from data acquired by onboard sensors and knowledge of its aerodynamics model only. We employ two complementary methods. The first is based on the estimation of the external wrench (force and torque) due to aerodynamics acting on the robot in flight. Wind velocity is obtained by inverting an identified model of the aerodynamic forces. The second method is based on the estimation of the propeller aerodynamic power, and provides an estimate independent of other sensors. We show how to calculate components of the wind velocity using multiple aerodynamic power measurements, when the poses between them are known. The method uses the motor current and angular velocity as measured by the electronic speed controllers, essentially using the propellers as wind sensors. Verification of the methods and model identification were done using measurements acquired during autonomous flights in a 3D wind tunnel.

I. INTRODUCTION

The small size and cost of multicopters makes them a good candidate as versatile, flying wind sensors. Wind field estimation has already been demonstrated in fixed-wing UAVs [1], [2]. A pitot tube is used to measure the relative airspeed, which is compared to the GPS-based ground speed to obtain the wind velocity. Pressure probes can also be used on quadcopters to obtain the airspeed [3], [4], [5]. However, it is more common to use an aerodynamics model for this purpose [6], [7], [8], [9]. Together with increasingly available localization in unknown, GPS-denied environments [10], [11], these systems can be used for autonomous wind field mapping.

Contribution. In this paper, we propose a novel method to estimate the wind velocity based on momentum theory, using only propeller power measurements. The propellers are thereby used as wind sensors. We compare this method to a linear and a neural network model of the aerodynamic forces, which are estimated by an external wrench observer [12]. To identify the model and verify the methods, we flew a custom hexacopter in the world’s first 3D wind tunnel [13], as depicted in Fig. 1. To the best of our knowledge, this is the first such experiment. We test our methods using experimental data. The power-based method presented in



Fig. 1: Experimental verification of the presented methods is done by flying a coaxial hexacopter in a 3D wind tunnel. The hexacopter hovers autonomously using a position controller, based on pose measurements from an external tracking system. For comparison, we also log data from a stereo vision based onboard pose estimator. Depicted is flow visualization at a wind velocity of around 6 m/s. We loosely suspend the robot with a filament for safety purposes.

this paper opens new applications. It can be used as a wind velocity measurement that is complementary to the commonly used external wrench based estimation. The independent measurement could be used to distinguish between aerodynamic and contact forces, which is not possible when using only external wrench information [9]. Furthermore, it could be used to enhance MAV state estimation. We can also use it to map wind velocities in a small area [14], and perform aerodynamics-aware trajectory planning.

Related work. The freestream velocity of multicopter MAVs is commonly obtained from accelerometer measurements. This can be done because the propeller induced drag and blade flapping produce a horizontal force that can be measured by the onboard accelerometer. However, only the horizontal velocity components can be obtained that way. Waslander and Wang [6] used a linear drag model and the propeller model from [15] to estimate the wind velocity. Due to complexity of wind-dependent thrust calculations, estimation of the vertical wind component had limited accuracy. This paper showed the feasibility of model-based wind estimation. The same effect was used by Martin *et al.* [7] and Abeywardena *et al.* [16] to estimate the relative airspeed of a quadcopter. This aerodynamics model has also been used to improve controller performance for aggressive maneuvers by Huang *et al.* [15] and in a nonlinear control scheme by Omari *et al.* [8]. The wind velocity and yaw rates of the vehicle were neglected. Alternatively, Yeo *et al.* [4], [5] and Sydney *et al.* [3] have used airspeed probes to measure the freestream velocity of a quadcopter. They used this measurement to map the wind field and improve controller performance. Bangura

¹ {teodor.tomic, philipp.lutz}@dlr.de, German Aerospace Center (DLR), Robotics and Mechatronics Center (RMC), Münchner Straße 20, 82234 Weßling, Germany

² korbinian.schmid@roboception.de, Roboception GmbH, Kafflerstr. 2, 81241 Munich, Germany

³ amather5@uwo.ca, WindEEE Research Institute, 2535 Advanced Avenue, London, ON, Canada

⁴ sami.haddadin@irt.uni-hannover.de, Institut für Regelungstechnik, Leibniz Universität Hannover, Appelstr. 11, 30167 Hannover, Germany

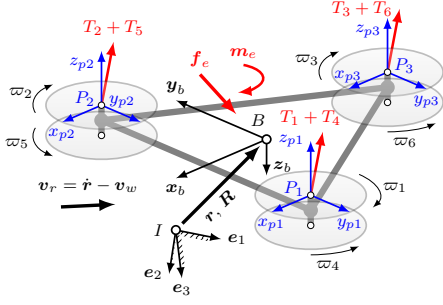


Fig. 2: Free-body diagram of the coaxial hexacopter used in the experiments. The body frame B is located at position \mathbf{r} and orientation \mathbf{R} in the inertial frame I and subject to wind velocity \mathbf{v}_w . This causes the external wrench $\boldsymbol{\tau}_e = [\mathbf{f}_e^T \mathbf{m}_e^T]^T$ due to aerodynamic forces dependent on the airspeed \mathbf{v}_r . The propellers rotating at angular velocities $\boldsymbol{\omega} = [\omega_1 \dots \omega_6]^T$ generate the control wrench $\boldsymbol{\tau} = [\mathbf{f}^T \mathbf{m}^T]^T$ through the thrusts T_i and drag torques Q_i . The propeller frames $P_{1,2,3}$ are depicted in blue.

et al. [17], [18] used momentum theory [19] to estimate and control the propeller aerodynamic power, which is directly related to thrust. Furthermore, they used the estimated aerodynamic power to estimate the propeller thrust with known freestream velocity. In our previous work [9] we showed how to incorporate blade flapping and momentum theory into external wrench estimation and collision detection.

In order to verify aerodynamics models, other authors have carried out static wind tunnel measurements. Schiano *et al.* [20] and Planckaert *et al.* [21] measured the forces and torques acting on a static quadrotor under varying conditions. Marino *et al.* [22] measured the motor power in steady-state wind conditions and related it to the wind velocity. They found that the mapping of power to wind velocity is not unique, and the solution quality varies with the flow conditions. However, no online estimation scheme was proposed.

This paper is organized as follows. In Section II we review the relevant mathematical models. In Section III we propose two methods to estimate the wind velocity. The first method models wind velocity as a function of the estimated external forces. The second method uses multiple propeller power measurements and momentum theory in a nonlinear least squares formulation. The experimental setup is described in Section IV, and results are shown in Section IV-C. Lastly, we conclude in Section V.

II. PRELIMINARIES

A. Rigid-body dynamics

A free-body diagram of a coaxial hexacopter is depicted in Fig. 2. The equations of motion can be written as

$$\mathcal{M}\ddot{\mathbf{r}} = \mathcal{M}g\mathbf{e}_3 + \mathbf{R}\mathbf{f} + \mathbf{R}\mathbf{f}_e \quad (1)$$

$$\mathcal{I}\dot{\boldsymbol{\omega}} = (\mathcal{I}\boldsymbol{\omega}) \times \boldsymbol{\omega} - \mathcal{M}g(\mathbf{r}_g) \times \mathbf{R}^T\mathbf{e}_3 + \mathbf{m} + \mathbf{m}_e \quad (2)$$

$$\dot{\mathbf{R}} = \mathbf{R}(\boldsymbol{\omega}) \times \quad (3)$$

where \mathcal{M} is the robot mass, $\mathbf{r} = [x, y, z]^T$ is its position in the fixed North-East-Down (NED) inertial frame, $\mathbf{R} \in SO(3)$ is the rotation matrix from the body to the

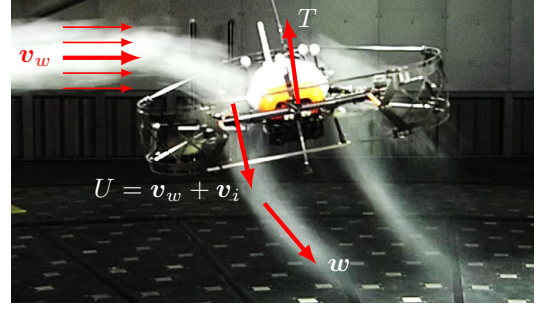


Fig. 3: Thrust T is generated by increasing the wind velocity \mathbf{v}_w by the propeller induced velocity \mathbf{v}_i , which goes through the propeller normal. The propeller slipstream finally merges into the wind flow to produce \mathbf{w} .

inertial frame, $\mathcal{I} \in \mathbb{R}^{3 \times 3}$ is its moment of inertia, $(\cdot) \times$ is skew-symmetric matrix operator, g is the acceleration of gravity, $\boldsymbol{\omega}$ is the body angular velocity, \mathbf{e}_3 is the z -axis unit vector, \mathbf{r}_g is the location of the center of gravity, \mathbf{f} and \mathbf{f}_e are the body-frame control and external forces, and \mathbf{m} and \mathbf{m}_e are the control and external torques, respectively. We denote the control wrench as $\boldsymbol{\tau} = [\mathbf{f}^T \mathbf{m}^T]^T$, and the external wrench as $\boldsymbol{\tau}_e = [\mathbf{f}_e^T \mathbf{m}_e^T]^T$. In general, $\boldsymbol{\tau}$ depends on the freestream velocity \mathbf{v}_∞ and propeller speeds $\boldsymbol{\omega}$ [9].

B. External wrench estimation

Here we briefly revisit the external wrench estimator from [12]. The estimator uses the control input, a system model and proprioceptive sensors only. The external wrench estimate $\hat{\boldsymbol{\tau}}_e = [\hat{\mathbf{f}}_e^T \hat{\mathbf{m}}_e^T]^T$ is obtained from

$$\hat{\boldsymbol{\tau}}_e = \begin{bmatrix} \int \mathbf{K}_I^f \left(\mathcal{M}\mathbf{a} - \mathbf{f} - \hat{\mathbf{f}}_e \right) dt \\ \mathbf{K}_I^m \left(\mathcal{I}\boldsymbol{\omega} - \int_0^t (\mathbf{m} + (\mathcal{I}\boldsymbol{\omega}) \times \boldsymbol{\omega} - \hat{\mathbf{m}}_e) dt \right) \end{bmatrix}, \quad (4)$$

where \mathbf{K}_I^f and \mathbf{K}_I^m are the filter gains, $\mathbf{a} = \mathbf{R}^T(\ddot{\mathbf{r}} - g\mathbf{e}_3)$ is the acceleration measured by an accelerometer in the center of mass expressed in the body frame, and $\hat{\mathbf{f}}_e$ and $\hat{\mathbf{m}}_e$ are the estimated external force and torque, also expressed in the body frame. The estimation dynamics are shown to be $(s + K_I)\hat{\boldsymbol{\tau}}_e = K_I\boldsymbol{\tau}_e$. In contrast to e.g. [23], [24], this estimator does not require translational velocity measurements.

C. Propeller aerodynamics

The forces exerted by a propeller depend on its freestream velocity (relative wind velocity). The freestream velocity of the k -th propeller expressed in the propeller frame is

$$\mathbf{v}_\infty^{(k)} = \mathbf{R}_{pb}^{(k)} \left(\mathbf{R}^T \mathbf{v}_r + \boldsymbol{\omega} \times \mathbf{r}_k \right), \quad (5)$$

where $\mathbf{v}_r = \dot{\mathbf{r}} - \mathbf{v}_w$ is the true airspeed, \mathbf{v}_w is the wind velocity, $\mathbf{R}_{pb}^{(k)}$ is the rotation matrix from the body to the propeller frame and \mathbf{r}_k is the location of the propeller relative to the center of gravity. The thrust acts in positive z -direction of the propeller frame P_k , see Fig. 2. According to momentum theory [19] it can be written as

$$T = 2\rho A v_i U, \quad (6)$$

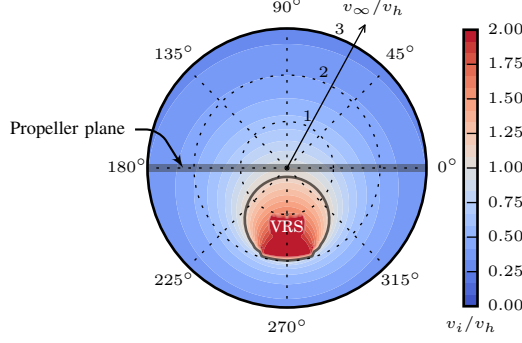


Fig. 4: Relative induced velocity v_i/v_h in forward flight, depending on angle of attack and relative airspeed v_∞/v_h , depicted on the radial axis. Unmodified momentum theory is invalid in the delineated area, where the propeller is in the Vortex Ring State (VRS) [19].

where ρ is the air density, A is the rotor disk surface area, and $U = \|v_i e_3 + v_\infty\|$ is the velocity of the propeller slipstream. The induced velocity v_i can be obtained using

$$v_i = v_h^2 / \sqrt{v_{xy}^2 + (v_i - v_z)^2}, \quad (7)$$

which may be solved by several Newton-Raphson iterations with known v_h and v_∞ [19]. A flow visualization of thrust generation and the relevant velocities is depicted in Fig. 3. The horizontal and vertical components of the freestream velocity are $v_{xy} = v_\infty - v_z$ and $v_z = e_3^T v_\infty$, respectively. Their norms are $v_{xy} = \|v_{xy}\|$ and $v_z = \|v_z\|$. In hover conditions the induced velocity is $v_h = \sqrt{T_h/2\rho A}$, where the hover thrust is $T_h = \rho D^4 C_T \omega^2$. The thrust coefficient C_T can be obtained from static thrust measurements, D is the propeller diameter, and ω is the propeller speed. The propeller ideal aerodynamic power is

$$P_a = 2\rho A v_i U (v_i - v_z). \quad (8)$$

Furthermore, the aerodynamic power in forward flight is related to the hovering power following

$$P_a/P_h = (v_i - v_z)/v_h, \quad (9)$$

with $P_h = 2\rho A v_h^3$. Nonidealities can be included through the figure of merit (FM), between 0 and 1, such that $P_a = P_m \cdot FM$, where P_m is the motor power. The theory must be applied in the valid domain. Unmodified momentum theory does not apply in the unsteady Vortex Ring State (VRS) [19], as depicted in Fig. 4.

D. Simplified brushless DC motor model

In order to estimate the propeller aerodynamic power, we employ the BLDC motor model from [18]. The mechanical part of motor dynamics can be represented by

$$\tau_m = (K_{q0} - K_{q1} i_a) i_a, \quad (10)$$

$$I_r \dot{\omega} = \tau_m - D_r, \quad (11)$$

where i_a is the current through the motor, and ω is the rotor angular velocity. The motor torque is τ_m , with the torque constant modeled as $K_q(i_a) = (K_{q0} - K_{q1} i_a)$. The

parameter I_r is the rotor inertia, and D_r is the aerodynamic drag torque acting on the rotor. The total motor mechanical power is $P_m = P_a/FM + P_r$, where the mechanical power P_m and power consumed by rotor acceleration P_r are used to estimate the aerodynamic power using

$$P_m = \tau_m \omega = (K_{q0} - K_{q1} i_a) i_a \omega, \quad (12)$$

$$P_r = I_r \omega \dot{\omega}, \quad (13)$$

$$\hat{P}_a = FM \left((K_{q0} - K_{q1} i_a) i_a - I_r \dot{\omega} \right) \omega. \quad (14)$$

In summary, we need to estimate or measure the motor current i_a , rotor speed ω and rotor acceleration $\dot{\omega}$. The measurements i_a and ω can be obtained from modern ESCs, and $\dot{\omega}$ can be estimated [18].

III. WIND VELOCITY ESTIMATION

Previous work has shown that the dominant horizontal force in multicopters is due to propeller induced drag [6]. Therefore, the external torques will be small and can be neglected for wind velocity estimation. When estimating wind from motor power, we expect high sensitivity of the estimated horizontal wind velocity component to noise in the motor power measurements. This is due to near-hovering flight conditions (low forward flight velocity) and the coplanar configuration and of our propellers. Furthermore, we will not be able to directly apply this method to our coaxial configuration, as this is not accurately described by momentum theory.

A. Wind velocity from external wrench measurements

We may obtain the wind velocity from the external wrench τ_e acting on the robot. Assuming $\tau_e = \tau_d$, we need to invert the aerodynamics model $\tau_d = d(v_r)$. For simple models, this can be achieved by simple relations [8], or iteration [9].

Linear model. The widely used induced-drag and blade flapping model [8] can be written as

$$d(v_r) = D_l v_r \sum \omega_i, \quad (15)$$

where D_l is the linear coefficient matrix. By applying $f_e = d(v_r)$, we may write

$$v_r(d) = \frac{1}{\sum \omega_i} D f_e, \quad (16)$$

where D is a coefficient matrix. This model implicitly assumes that the flying robot has a symmetrical shape.

Learning-based approach. We may also model the relation using a Radial Basis Function (RBF) neural network. This has the advantage that the inverse relation can be directly encoded into the RBF. However, the number of basis functions, their centers and shape parameters also have to be tuned. We model the relation $v_r = d^{-1}(\tau_e)$ as a normalized RBF network with K basis functions

$$v_r = \frac{1}{\phi_\Sigma} W \phi(\tau_e), \quad (17)$$

where the matrix $W \in \mathbb{R}^{3 \times K}$ contains weights of the RBFs for each velocity component

$$W = \begin{bmatrix} w_x^T \\ w_y^T \\ w_z^T \end{bmatrix} = \begin{bmatrix} W_{x,1} & \cdots & W_{x,K} \\ W_{y,1} & \cdots & W_{y,K} \\ W_{z,1} & \cdots & W_{z,K} \end{bmatrix}, \quad (18)$$

and the vector $\phi = [\phi(r_1), \dots, \phi(r_K)]^T$ is the vector of evaluated basis functions. The network is normalized by the factor $\phi_\Sigma = \sum_{i=1}^K \phi(r_i)$. We use the Gaussian basis function

$$\phi(r_i) = \exp\left(-\frac{1}{\sigma^2} \|\mathbf{x} - \mathbf{c}_i\|^2\right), \quad (19)$$

where σ is a shape parameter, \mathbf{x} is the evaluated vector, and \mathbf{c}_i is the center of the i -th basis function. In order to avoid the curse of dimensionality and for the norm to have physical meaning, we use only the external forces \mathbf{f}_e .

For learning the vector \mathbf{w}_i ; $i \in (x, y, z)$, we use a batch least squares approach of L measurements, such that $\mathbf{Y}\mathbf{w}_i = \mathbf{b}$, with $\mathbf{Y} \in \mathbb{R}^{L \times K}$ and $\mathbf{b} \in \mathbb{R}^L$ being

$$\mathbf{Y} = \begin{bmatrix} \phi_1(\mathbf{f}_{e,1}) & \cdots & \phi_K(\mathbf{f}_{e,1}) \\ \vdots & \ddots & \vdots \\ \phi_1(\mathbf{f}_{e,L}) & \cdots & \phi_K(\mathbf{f}_{e,L}) \end{bmatrix}, \quad \mathbf{b} = \begin{bmatrix} v_{r,i,1} \\ \vdots \\ v_{r,i,L} \end{bmatrix}. \quad (20)$$

With this approach we can easily include additional information, for example aerodynamic power. We may thus learn $\mathbf{v}_r = \mathbf{f}(\tau_e, P_a/P_h)$. There is also no assumption on the shape of the robot. However, a lot of data is needed for learning, and the model does not generalize well.

B. Wind velocity from aerodynamic power measurements

In this section, we present a novel method to obtain wind velocity from aerodynamic power measurements, based on momentum theory. We start by rewriting the aerodynamics of one propeller (7), (8) and (9) as a system of nonlinear equations $\mathbf{F}(v_i, v_z, v_{xy}, v_h, P_a) = \mathbf{0}$, with $\mathbf{F} = [F_1, F_2, F_3]^T$, where

$$\begin{aligned} F_1 &= v_i^4 - 2v_i^3 v_z + v_i^2(v_z^2 + v_{xy}^2) - v_h^4 = 0, \\ F_2 &= v_i U(v_i - v_z) - P_a/(2\rho A) = 0, \\ F_3 &= v_h^2(v_i - v_z) - P_a/(2\rho A) = 0. \end{aligned} \quad (21)$$

We consider $P_a/(2\rho A)$ and v_h to be known inputs, and want to determine $\mathbf{x} = [v_x, v_y, v_z, v_i]^T$. This system of nonlinear equations is underdetermined, as we have two knowns and three unknowns, since v_x and v_y are coupled in v_{xy} . Due to this mapping, the solution of (21) will be a manifold, and depends on the initial guess. Hence, we cannot use (21) to uniquely determine the unknowns. To solve this problem, we expand the system of equations to include multiple measurements. We then introduce a transformation of (21) into a common frame. This allows us to estimate all three wind velocity components and the propeller induced velocities by solving a nonlinear least squares (NLS) problem.

Multiple measurements. Let us assume a constant wind velocity $\mathbf{v}_w = [v_x, v_y, v_z]^T$ through N measurements. This assumption holds in several cases. First, we can combine instantaneous measurements from multiple propellers that are rigidly attached (e.g. quadcopter). These may also be rotated w.r.t. the body frame. Second, we can combine measurements from multiple poses at different time instants in a small time window. Third, if the flight is not aggressive, i.e. the orientation does not change significantly, we can estimate the body-frame freestream velocity. In effect, we

use information gained from N measurements to obtain the wind velocity components.

We may extend the state to N measurements

$$\mathbf{x} = [v_x, v_y, v_z, v_i^{(1)}, v_i^{(2)}, \dots, v_i^{(N)}]^T, \quad (22)$$

and solve the extended system of equations

$$\begin{aligned} \mathbf{F}(v_x, v_y, v_z, v_i^{(1)}, v_h^{(1)}, P_a^{(1)}, \dots, v_i^{(N)}, v_h^{(N)}, P_a^{(N)}) &= \mathbf{0}, \\ \mathbf{F} &= [F_1^{(1)}, F_2^{(1)}, F_3^{(1)}, \dots, F_1^{(N)}, F_2^{(N)}, F_3^{(N)}]^T, \end{aligned} \quad (23)$$

where $F_1^{(k)}$, $F_2^{(k)}$ and $F_3^{(k)}$ are evaluations of (21) for the k -th measurement. A Jacobian is needed to solve (23). The Jacobian for the k -th measurement is defined as

$$\mathbf{J}^{(k)} = \begin{bmatrix} J_{11}^{(k)} & J_{12}^{(k)} & J_{13}^{(k)} & J_{14}^{(k)} \\ J_{21}^{(k)} & J_{22}^{(k)} & J_{23}^{(k)} & J_{24}^{(k)} \\ J_{31}^{(k)} & J_{32}^{(k)} & J_{33}^{(k)} & J_{34}^{(k)} \end{bmatrix}, \quad (24)$$

where $J_{ij}^{(k)} = \partial F_i^{(k)} / \partial x_j^{(k)}$. We can now construct the extended Jacobian $\mathbf{J}|_N \in \mathbb{R}^{3N \times N+3}$. For three measurements we have $\mathbf{x}|_{N=3} = [v_x, v_y, v_z, v_{i,1}, v_{i,2}, v_{i,3}]^T$ and

$$\mathbf{J}|_{N=3} = \begin{bmatrix} J_{11}^{(1)} & J_{12}^{(1)} & J_{13}^{(1)} & J_{14}^{(1)} & 0 & 0 \\ J_{21}^{(1)} & J_{22}^{(1)} & J_{23}^{(1)} & J_{24}^{(1)} & 0 & 0 \\ J_{31}^{(1)} & J_{32}^{(1)} & J_{33}^{(1)} & J_{34}^{(1)} & 0 & 0 \\ J_{11}^{(2)} & J_{12}^{(2)} & J_{13}^{(2)} & 0 & J_{14}^{(2)} & 0 \\ J_{21}^{(2)} & J_{22}^{(2)} & J_{23}^{(2)} & 0 & J_{24}^{(2)} & 0 \\ J_{31}^{(2)} & J_{32}^{(2)} & J_{33}^{(2)} & 0 & J_{34}^{(2)} & 0 \\ J_{11}^{(3)} & J_{12}^{(3)} & J_{13}^{(3)} & 0 & 0 & J_{14}^{(3)} \\ J_{21}^{(3)} & J_{22}^{(3)} & J_{23}^{(3)} & 0 & 0 & J_{24}^{(3)} \\ J_{31}^{(3)} & J_{32}^{(3)} & J_{33}^{(3)} & 0 & 0 & J_{34}^{(3)} \end{bmatrix},$$

which is straightforward to extend to N measurements.

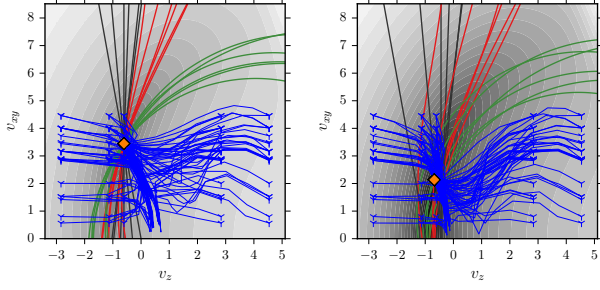
Transformed formulation. When combining measurements from different poses, the wind velocity has to be transformed into a common coordinate frame. Otherwise, the constant wind velocity assumption will not hold. Define the freestream velocity of propeller k as

$$\mathbf{v}^{(k)} = \begin{bmatrix} v_x^{(k)} \\ v_y^{(k)} \\ v_z^{(k)} \end{bmatrix} = \mathbf{R}^{(k)} \begin{bmatrix} v_x \\ v_y \\ v_z \end{bmatrix} + \mathbf{v}_0^{(k)}, \quad (25)$$

and use the transformed velocities when calculating (21) and (24). The offset velocity $\mathbf{v}_0^{(k)}$ can be obtained from a pose estimation system as the delta velocity between two measurements. We may also use the propeller offset velocity due to the body angular velocity, i.e. $\mathbf{v}_0^{(k)} = \mathbf{R}_{pb}^{(k)} \boldsymbol{\omega} \times \mathbf{r}_k$.

This formulation allows us to determine all three components of the freestream velocity independently. It also allows to obtain the instantaneous wind velocity components when the propellers are not mounted to the multicopter frame in a coplanar configuration.

Solving the system of equations. When the equations match, we solve a multidimensional root-finding problem. The solution will then be at the intersection of all nonlinear functions, where $\mathbf{F} = \mathbf{0}$. However, under model mismatch,



(a) No noise in P_a , at real v_i (b) Noise in P_a , converged v_i

Fig. 5: Zero contours of (26), with color indicating the function value. Green lines are contours of $F_1^{(k)}$, red lines are contours of $F_2^{(k)}$, and black lines are contours of $F_3^{(k)}$ at $v_i = \text{const}$. The blue lines show convergence of a Levenberg-Marquardt solver for different initial guesses. The converged solution is depicted as an orange diamond. The velocity components v_x and v_y lumped into v_{xy} . We used $N = 6$ measurements, velocity $v_\infty = 3.5$ m/s, angle of attack $\alpha = 10^\circ$, $v_h \in [4.1 \dots 6.7]$ m/s, and measurement angles up to 10° . Without noise on the power measurement (Fig. 5(a)), the solution converges to the exact wind velocity $\mathbf{v}_w = [-3.45, 0 - 0.61]^T$ m/s. With noise in the power measurements, the least-squares solution moves depending on measurement conditioning.

i. e. when the measured aerodynamic power does not match momentum theory, the functions will not necessarily intersect. In this case we have to solve a nonlinear least squares problem with the objective function

$$f = \frac{1}{2} \mathbf{F}^T \mathbf{F}, \quad (26)$$

for example using a Levenberg-Marquardt solver [25], [26].

When an exact solution exists, it will be at $f = 0$, i. e. the intersection of $\mathbf{F} = \mathbf{0}$. Otherwise, if there is a model mismatch or noise in P_a , we get a least squares solution. Fig. 5 shows convergence of the solver for different initial guesses and noise on P_a .

Limiting the search space. The space of (26) can contain local optima. From the underlying physics, the same measured power can be obtained by various wind and induced velocities. The optimized variables are velocities. We may therefore use physical considerations to determine the set of feasible solutions. A flying robot must expend power to generate thrust, which implies $T > 0$ and $P_a > 0$, for which we use (6) and (8), respectively. The induced velocity is $v_i < v_h$ in the normal working state, and $v_i > v_h$ in the VRS. We exclude VRS from the search space because momentum theory is invalid in that state. Therefore, we limit induced velocity to $0 < v_i < v_h$. Likewise, we can limit \mathbf{v}_w in case of knowledge of its limits. In order to limit the search space using the Levenberg-Marquardt method, we add a quadratic barrier function F_4 to the optimization problem formulation [25], which increases the size of the problem, as the function becomes $\mathbf{F} \in \mathbb{R}^{4N}$, and the Jacobian becomes $\mathbf{J}|_N \in \mathbb{R}^{4N \times N+3}$.

Normalization. In order to improve stability of the numerical solution, we normalize the goal function to its initial value J_0 , i. e. we minimize $J' = J_0^{-1} J$. Furthermore, the functions $F_{1...3}^{(k)}$ are normalized to $v_h^{(k)}$, such that

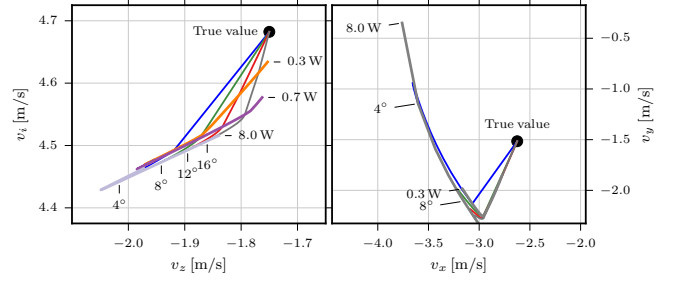


Fig. 6: Sensitivity of the NLS solution to error in aerodynamic power \hat{P}_a up to 8 W, using $N = 12$ measurements, and maximum measurement angles σ_α up to 20° . For $\sigma_\alpha = 0^\circ$, the solution diverges out of plot and is not shown. Wind speed is $v_\infty = 3.5$ m/s. Larger measurement angles lead to a more robust solution, as the estimated wind velocity is closer to the real value even for high errors in the aerodynamic power. The vertical wind component v_z and propeller induced velocity v_i are estimated with good accuracy for a wide range of \hat{P}_a . However, the horizontal wind components v_x , v_y diverge from their real values even for low \hat{P}_a .

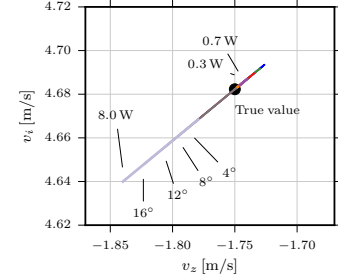


Fig. 7: Sensitivity of the NLS solution for the same case as in Fig. 6, but for perfect knowledge of horizontal velocity components (v_x , v_y), which may be obtained from the induced drag model, i. e. the external force. When the horizontal wind velocity is known, the vertical component can be determined robustly from the aerodynamic power measurements.

$F'_1 = F_1/v_h^4$, $F'_2 = F_2/v_h^3$, $F'_3 = F_3/v_h^3$, $F'_4 = F_4/v_h^2$. In this way, the function values are dimensionless and have the same order of magnitude.

Sensitivity analysis. Measurement noise will shift the estimated wind velocity in a nonlinear manner, as can be seen in Fig. 5. We therefore perform a sensitivity analysis to estimate this effect. Figure 6 depicts the converged solutions for increasing noise amplitude in the measured power. Since the quality of the solution will depend on the distribution of measurement poses, we uniformly distribute these under different maximum angles, from 5° to 20° . Higher relative angles between measurement poses increase robustness of the solution. However, estimation of the horizontal wind velocity components is very sensitive to power measurements.

We therefore propose to estimate the horizontal velocity components using the induced drag model, i. e. from the external force. As shown in Fig. 7, this allows a robust estimation of the vertical wind velocity component and the propeller induced velocity even for a high error in power measurements. A minimum angular distance between measurements should also be considered when choosing suitable measurements for the NLS problem. Having an offset velocity \mathbf{v}_0 in (25) additionally reduces sensitivity to noise in the power measurements.

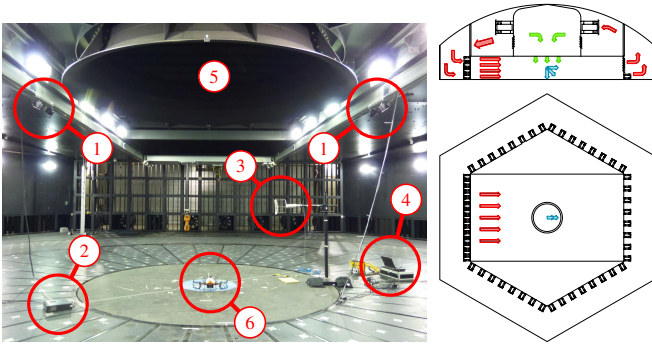


Fig. 8: Left: experimental setup inside the wind tunnel: four ART Tracking cameras (1) and ART controller (2), RM Young Model 81000 Sonic Anemometer (3), groundstation laptop (4). Vanes (5) are used to generate the vertical wind component. The flying robot (6) is located in the center of the flying area. Right: schematic layout of the wind tunnel test. Red arrows show horizontal flow component, green arrows show vertical flow component, blue arrows show net wind vector.

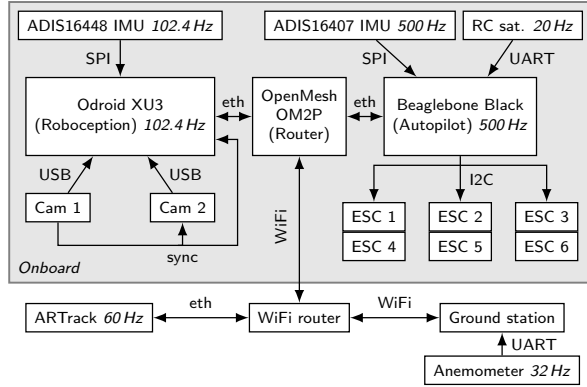


Fig. 9: Experiment hardware setup. We use a Beaglebone Black running a Linux with realtime patch as the autopilot. The Odroid XU-3 is used as the onboard pose estimator, with a separate IMU and triggered stereo cameras. They are connected through an onboard wireless router, which also serves as a connection to the groundstation.

C. Combined wind estimator

In order to overcome limitations of the two presented methods, we propose a combined wind estimator. The horizontal velocity components (v_x, v_y) are obtained from the external wrench, using (16) or (17). We then use the estimated aerodynamic power and known (v_x, v_y) to calculate v_z using the nonlinear least squares formulation, by minimizing the cost function (26). We note that this optimization may also be implemented as a nonlinear filter for online estimation, however this the subject of future work.

IV. EXPERIMENTAL SETUP AND RESULTS

A. Flying robot platform

Hardware. The experiments were carried out using a custom-built hexacopter in a coaxial configuration. For propulsion we used six identical T-Motor MN2212 920 Kv motors at a 4S voltage (14.8V), with T-Motor CF 10x3.3 propellers. The computational hardware setup is outlined in Fig. 9. A Beaglebone Black with realtime Linux is used as the autopilot. We use ESC32v2 speed controllers with

firmware modified to support I2C communication. The ESCs measure the motor current using a shunt resistor. An Odroid XU3 is used for onboard pose estimation by fusing stereo visual odometry and IMU data. The two PointGrey Firefly cameras are synchronized with a hardware trigger. Communication between the two onboard computers is achieved over Ethernet through a wireless router, which is also used as connection with the groundstation.

Software. The orientation strapdown, attitude and position controllers run on the autopilot computer at 500 Hz. The motor feedback is obtained at 1/6th of the control rate. Pose updates are sent to the autopilot either from the groundstation (motion capture system) or the Odroid (onboard pose estimation). The received poses are used for position and attitude control. Communication between components is done using a custom real-time capable middleware, over shared memory and UDP. For onboard pose estimation we employ a Roboception [27] Navigation Sensor which exposes the full 6D pose of the robot, its velocities as well as unbiased IMU measurements. The state estimator fuses keyframe delta poses of a stereo vision odometry with IMU measurements by an indirect, extended Kalman filter while latencies of the vision system are compensated [11]. The whole pipeline runs on the on-board Odroid XU3 computer.

B. Wind tunnel

The Wind Engineering, Energy and Environment (WindEEE) Dome, see Hangan [13], is the world's first 3D wind chamber, consisting of a hexagonal test area 25 m in diameter and an outer return dome 40 m in diameter. Mounted on the peripheral walls and on top of the test chamber are a total of 106 individually controlled fans and 202 louver systems. Additional subsystems, including an active boundary layer floor and "guillotine" allow for further manipulation of the flow. These are integrated via a sophisticated control system which allows dynamic manipulation with thousands of degrees of freedom to produce various time and spatially dependent flows including straight uniform, atmospheric boundary layer, shear gusts, downbursts and tornados at multiple scales. A pair of 5 m diameter turntables allow for a wide variety of objects to be tested inside and outside the facility.

For this project WindEEE was configured to produce straight flow closed-loop and downburst flows concurrently. In this configuration the test area was restricted to a 4.5 m diameter, 3.8 m tall region at the centre of the facility. See Fig. 8 for a schematic drawing of the layout. A rectangular array of 36 fans (9 wide by 4 high) located on the south chamber wall were used to produce horizontal flow and 6 large fans above the test chamber were used to generate the downward flow. The respective flow rates from the horizontal and vertical component fans were manipulated individually to generate net wind vectors ranging in velocity from 1–5 m/s and vertical plane angularity from 0–90°. In some cases both the velocity and vertical plane angularity were manipulated dynamically to produce time-dependent wind vectors that either varied in speed or angularity over a given test run.

TABLE I: Identified system parameters. Upper and lower propellers have different thrust and torque coefficients. The nondiagonal elements of \mathcal{I} are two orders of magnitude smaller than the diagonal elements, and are therefore neglected.

Parameter	Value
Mass	\mathcal{M} 2.445 kg
Inertia	$\mathcal{I}_{\text{diag}}$ $[27.3, 25.3, 27.6]^T \cdot 10^{-3} \text{ kg m}^2$
Center of mass	\mathbf{r}_g $[-0.46, 0.11, 1.25]^T \cdot 10^{-2} \text{ m}$
Thrust coef.	C_T 0.0048 (upper), 0.0058 (lower)
Torque const.	K_{q0} $1.038 \cdot 10^{-2} \text{ N m/A}$
Rotor inertia	I_r $2.235 \cdot 10^{-5} \text{ kg m}^2$

C. Results

For training aerodynamic models, we flew in horizontal, vertical and combined wind flows with varying wind velocities. The flying robot was hovering in position controlled mode and was rotated about the yaw axis. We combined several flights into a single training set, depicted in Fig. 10. The algorithms were verified offline. Where necessary, data was smoothed using a convolution filter without delay.

Parameter estimation. The system parameters were first identified and verified in identification flights without wind influence. For inertial parameters, we used a batch least squares approach with a linear parameterization of the system dynamics. We used the known mass to compute the gravity wrench. The control input was obtained from the measured propeller speeds. Table I lists the resulting parameters.

Horizontal velocity estimation. As can be seen from Fig. 11, both the linear model (LM) and radial basis function (RBF) learning-based approach can estimate the horizontal velocity from the external force with good accuracy. The LM results in a full 3×3 matrix. For the RBF we used 64 centers. Therefore, it is able to estimate the vertical wind component better than the simple model. We found that using motor power data ($\hat{P}_a^\Sigma / P_h^\Sigma$ in Fig. 10) did not improve the accuracy of the RBF network. The experimental data is therefore omitted for brevity.

Motor power. In order to test if using motor power in the RBF improves accuracy, we used the total measured motor powers normalized to the expected power in hovering. As shown in Fig. 10, this approach coincides well with momentum theory. However, it does not work for individual propellers, as the effect of coaxial rotors is not modeled. We therefore do not expect good results from the NLS approach when applying the measured power. Note that this is only a limitation of our hexacopter, and not due to the method.

Obtaining wind velocity from motor power. When the horizontal velocity components are known, the NLS momentum theory formulation presented in Section III-B accurately reconstructs the vertical component. Using the horizontal velocity obtained from the RBF still provides good results, as can be seen in Fig. 11. Here we used the four previous measurements of the top propellers, i.e. $N = 12$. Results of the combined wind estimator are similar to RBF approach, and are limited by the accuracy of the horizontal velocity estimation, and accuracy of the aerodynamic power model. The power-based wind estimation may therefore be seen as complementary to the learning-based approach.

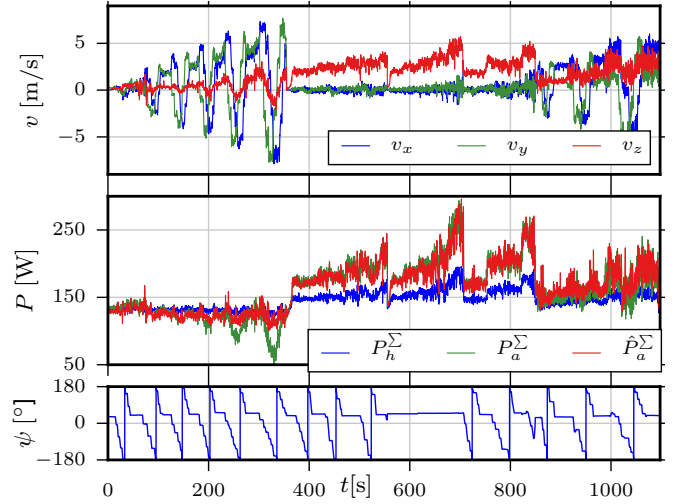


Fig. 10: The training set for aerodynamics models contains 18 minutes of flight data under horizontal wind speed up to 8 m/s, and vertical wind speeds up to 5 m/s. Higher vertical wind speeds were not possible due to actuator saturation and loss of yaw control authority. The relative airspeed in the body frame is depicted. We varied the yaw angle throughout the flights. The middle plot shows the sum of powers of the six motors. The hover power is obtained from $P_h = 2\rho A v_h^3$. The expected aerodynamic power is P_a , with induced velocity calculated from (7) and (8), using the relative airspeed obtained from the anemometer data and external tracking system. Because momentum theory is not easily applicable to coaxial rotors, we fit the estimated aerodynamic power as $\hat{P}_a = P_0 + \beta P_m$, which provides a good fit with momentum theory.

V. CONCLUSION

In this paper, we presented methods to obtain wind velocity from two independent inputs, namely external wrench and motor power. The first method, which builds on our previous work, learns the drag model and inverts it for velocity estimation for this purpose. It assumes that drag is the only external wrench acting on the system. The scheme requires an IMU and known control inputs only. The second algorithm obtains wind velocity from aerodynamic power measurements only, which are easy to obtain by modern electronic speed controllers typically employed in multicopters. The method provides an estimate that is independent from the drag model and other external forces as e.g. contacts.

Both schemes were experimentally verified with a hexacopter in a 3D wind tunnel. To the authors' knowledge such an experiment was done for the first time. In summary, the following conclusions can be drawn. 1) The linear model utilizing the wrench observer provides similarly accurate results for the horizontal coordinates compared to the RBF approach, that works also on the external force/torque estimation. Additionally including power measurements did not improve these results. 2) If the horizontal velocity is known (either from wrench estimation or ground truth), the reconstruction of the vertical velocity works well. To sum up, the combination of both methods we developed results in a fully operational *flying anemometer*.

Next steps cover the execution of the schemes in real-time, a more thorough sensitivity analysis and the accurate modeling of the coupling effects due to coaxial rotors.

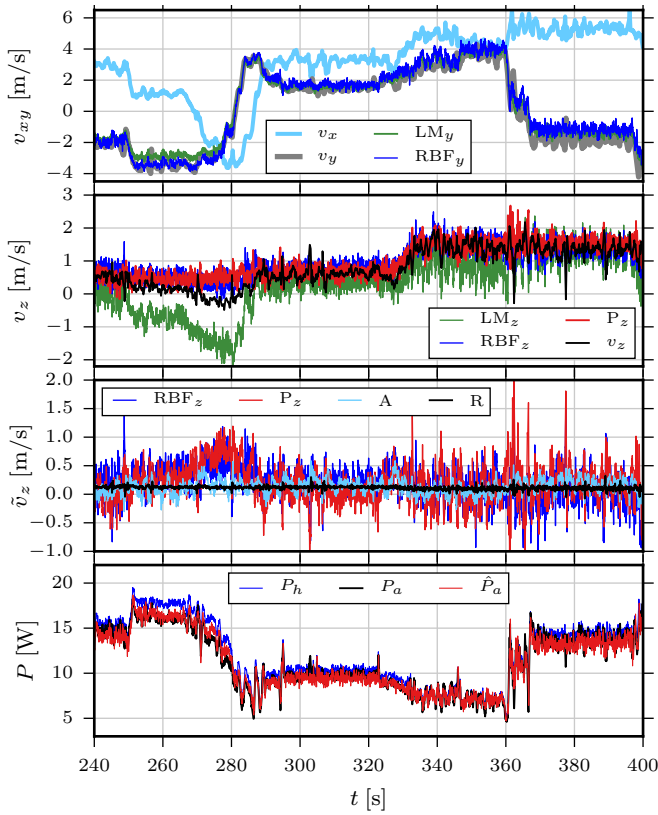


Fig. 11: Estimation of the body-frame relative airspeed, for a validation dataset. Ground Truth (v_x , v_y , v_z) is also shown. Top: The horizontal velocity is estimated using a Linear Model (LM) or Radial Basis Function (RBF). Performance for v_x is similar. The RBF has better accuracy than LM in the vertical (second row). Second and third row: vertical velocity v_z and estimation error \tilde{v}_z . In case (R), black, we use P_a obtained by momentum theory and ground truth horizontal velocity to *reconstruct* the vertical wind velocity v_z using NLS. For clarity, we only show the error. In case (A), cyan, we use the RBF-estimated horizontal velocity for reconstruction. In red (P_z) we employ the combined wind estimator, using the estimated aerodynamic power \hat{P}_a and RBF horizontal velocity. The discrepancy around $t = 275$ s presumably comes from unmodeled interaction effects of coaxial propellers. Fourth row: Aerodynamic power in hover (P_h), from momentum theory (P_a) and estimated from motor measurements ($\hat{P}_a = P_0 + \beta P_m$).

ACKNOWLEDGEMENTS

This work was partially funded by the project EuRoC (grant agreement no. CP-IP 608849). The authors would like to thank H. Wagner, R. Rittgarn, B. Pleitinger, F. Schmidt, T. Wüsthoff, I. Bargen and S. Moser for their support during development of the flying robot platform.

REFERENCES

- [1] J. W. Langelaan, N. Alley, and J. Neidhoefer, "Wind field estimation for small unmanned aerial vehicles," *Journal of Guidance, Control, and Dynamics*, vol. 34, no. 4, pp. 1016–1030, 2011.
- [2] S. Mayer, G. Hattenberger, P. Brisset, M. Jonassen, and J. Reuder, "A no-flow-sensor wind estimation algorithm for unmanned aerial systems," *International Journal of Micro Air Vehicles*, vol. 4, no. 1, pp. 15–30, 2012.
- [3] N. Sydney, B. Smyth, and D. Paley, "Dynamic control of autonomous quadrotor flight in an estimated wind field," in *CDC2013*, Dec 2013, pp. 3609–3616.
- [4] D. W. Yeo, N. Sydney, D. Paley, and D. Sofge, "Onboard flow sensing for downwash detection and avoidance with a small quadrotor helicopter," in *Proc. AIAA GNC Conference*, 2015.

- [5] D. W. Yeo, N. Sydney, and D. A. Paley, "Onboard Flow Sensing for Rotary-Wing UAV Pitch Control in Wind," in *Proc. AIAA GNC Conference*, 2016, p. 1386.
- [6] S. L. Waslander and C. Wang, "Wind Disturbance Estimation and Rejection for Quadrotor Position Control," in *AIAA Infotech@Aerospace Conference*, Seattle, WA, USA, April 6–9 2009.
- [7] P. Martin and E. Salaun, "The true role of accelerometer feedback in quadrotor control," in *ICRA 2010*, May 2010, pp. 1623–1629.
- [8] S. Omari, M.-D. Hua, G. Ducard, and T. Hamel, "Nonlinear Control of VTOL UAVs Incorporating Flapping Dynamics," in *IROS 2013*, Tokyo, Japan, November 2013, pp. 2419–2425.
- [9] T. Tomić and S. Haddadin, "Simultaneous estimation of aerodynamic and contact forces in flying robots: Applications to metric wind estimation and collision detection," in *ICRA 2015*, Seattle, WA, USA, May 2015, pp. 5290–5296.
- [10] K. Schmid, P. Lutz, T. Tomić, E. Mair, and H. Hirschl, "Autonomous vision-based micro air vehicle for indoor and outdoor navigation," *Journal of Field Robotics*, vol. 31, no. 4, pp. 537–570, 2014. [Online]. Available: <http://dx.doi.org/10.1002/rob.21506>
- [11] K. Schmid, F. Ruess, and D. Burschka, "Local reference filter for life-long vision aided inertial navigation," in *Information Fusion (FUSION)*, 2014 17th International Conference on. IEEE, 2014, pp. 1–8.
- [12] T. Tomić, "Evaluation of acceleration-based disturbance observation for multicopter control," in *Control Conference (ECC), 2014 European*, June 2014, pp. 2937–2944.
- [13] H. Hangan, "The Wind Engineering Energy and Environment (WindEEE) Dome at Western University, Canada," *Wind Engineers*, vol. 39, p. 350, 2014.
- [14] N. J. Sydney, "Rotorcraft Flight Dynamics and Control in Wind for Autonomous Sampling of Spatiotemporal Processes," Ph.D. dissertation, University of Maryland, 2015.
- [15] H. Huang, G. M. Hoffmann, S. L. Waslander, and C. J. Tomlin, "Aerodynamics and Control of Autonomous Quadrotor Helicopters in Aggressive Maneuvering," in *ICRA 2009*, Kobe, Japan, May 12–17 2009, pp. 3277–3282.
- [16] D. Abeywardena, Z. Wang, G. Dissanayake, S. L. Waslander, and S. Kodagoda, "Model-aided State Estimation for Quadrotor Micro Air Vehicles amidst Wind Disturbances," in *IROS 2014*, Chicago, IL, USA, Sep 14–18 2014, pp. 4813–4818.
- [17] M. Bangura and R. Mahony, "Nonlinear Dynamic Modeling for High Performance Control of a Quadrotor," in *Australasian Conference on Robotics and Automation, Proceedings of*, Wellington, New Zealand, Dec 3–5 2012.
- [18] M. Bangura, H. Lim, H. J. Kim, and R. Mahony, "Aerodynamic Power Control for Multirotor Aerial Vehicles," in *ICRA 2014*, Hong Kong, China, June 2014, pp. 529–536.
- [19] J. G. Leishman, *Principles of Helicopter Aerodynamics*, 2nd ed., ser. Cambridge Aerospace Series. Cambridge University Press, 2006.
- [20] F. Schiano, J. Alonso-Mora, K. Rudin, P. Beardsley, R. Siegwart, and B. Siciliano, "Towards Estimation and Correction of Wind Effects on a Quadrotor UAV," in *International Micro Aerial Vehicle Conference (IMAV)*, Delft, Netherlands, August 12–15 2014.
- [21] L. Planckaert and P. Coton, "Quadrotor UAV aerodynamic model identification using indoor flight experiment and feasibility of UAV as wind gust sensor," in *International Micro Aerial Vehicle Conference (IMAV)*, Aachen, Germany, Sep. 15–18 2015.
- [22] M. Marino, A. Fisher, R. Clothier, S. Watkins, S. Prudden, and C. S. Leung, "An Evaluation of Multi-Rotor Unmanned Aircraft as Flying Wind Sensors," in *International Micro Aerial Vehicle Conference (IMAV)*, Aachen, Germany, Sep. 15–18 2015.
- [23] F. Ruggiero, J. Cacace, H. Sadeghian, and V. Lippiello, "Impedance Control of VTOL UAVs with a Momentum-based External Generalized Forces Estimator," in *ICRA 2014*, Hong Kong, China, June 2014, pp. 2093–2099.
- [24] B. Yüksel, C. Secchi, H. H. Buelthoff, and A. Franchi, "A nonlinear force observer for quadrotors and application to physical interactive tasks," in *Advanced Intelligent Mechatronics, IEEE/ASME International Conference on 2014*, Besançon, France, July 8–11 2014.
- [25] J. Nocedal and S. Wright, *Numerical optimization*. Springer Science & Business Media, 2006.
- [26] S. Boyd and L. Vandenberghe, *Convex optimization*. Cambridge university press, 2004.
- [27] "Roboception GmbH," <http://www.robception.de>, [Online].